

Pulse optimization in adiabatic quantum computation and control

D. Turyansky,^{1,*} Y. Zolti,^{1,*} Y. Cohen,¹ and A. Pick^{1,†}

¹*Department of Applied Physics, The Hebrew University of Jerusalem, Jerusalem 9190401, Israel*

We present a pulse optimization method for accelerating adiabatic control protocols, including adiabatic population transfer and adiabatic quantum computation. Our method relies on identifying control pulses under which the evolving quantum system adheres to its instantaneous *adiabatic* ground state. Our method is both efficient—by using advanced gradient-free optimization tools and robust—by utilizing analytic adiabatic solutions in defining the cost function for quantum optimal control (QOC). To demonstrate the generality of our approach, we run digitized adiabatic protocols with superconducting qubits on the IBM quantum platform and numerically simulate adiabatic algorithms for solving graph optimization problems with Rydberg atom arrays.

We present a pulse optimization method for accelerating adiabatic control protocols, including adiabatic population transfer (APT) [48] and adiabatic quantum computation (AQC) [17], where a driven quantum system follows the instantaneous eigenstate of the Hamiltonian and reaches a desired target state (in APT) or the solution to a computational problem (in AQC). While adiabatic protocols are inherently robust to fluctuations in the controlling pulses, their speed is limited by the requirement that the system must change slowly compared to its spectral gap [2]. Therefore, accelerating adiabatic protocols [13, 19, 24] and adiabatic inspired computation paradigms [49] are a topic of active research. Motivated by the success of quantum optimal control (QOC) algorithms in enhancing the performance of gate-based quantum algorithms [16, 26], we introduce a QOC pulse-optimization method for adiabatic protocols. *Our method achieves optimal performance by minimizing leakage from the instantaneous eigenstate during the propagation, i.e., the “adiabatic error.”* The resulting pulses possess both high fidelity—by using QOC—and robustness—due to adherence to the instantaneous eigenstate.

By using the covariance matrix adaptation evolution strategy (CMA-ES) [23]—a stochastic gradient-free optimization algorithm—we efficiently optimize open multi-level many-body systems. To demonstrate our method, we study three examples: Rapid adiabatic passage in two-level systems (RAP), multi-level stimulated Raman adiabatic passage (STIRAP), and an AQC for solving a graph optimization problem. Our method finds robust RAP solutions more efficiently than brute force ensemble optimization [21]. Moreover, it is scalable, efficiently optimizing an AQC that involves 14 qubits.

According to the adiabatic theorem, suppressing diabatic errors requires control pulses to vary slowly compared to the spectral gap [6]. A common rule of thumb in adiabatic qubit control is that the product of the control pulse’s Rabi frequency, Ω , and its duration, t_f , should exceed 2π in order to substantially suppress diabatic

errors [38]. Although increasing Ωt_f indefinitely can, in principle, eliminate diabatic errors, practical limitations on time and energy necessitate educated pulse engineering. Squared trigonometric, hyperbolic, and smooth polynomial pulses are known to effectively minimize diabatic errors [35, 48]. Other methods for reducing diabatic errors include parallel-transported eigenvalues [22], superadiabatic states [33], and inertial pulses [14, 47]. A widely used acceleration technique called shortcut-to-adiabaticity [8] (STA) involves engineering counter-diabatic driving forces, which suppress diabatic transitions during the evolution [5]. While exact STA can eliminate diabatic errors altogether, its construction requires knowledge of all eigenstates and their derivatives [32]. When the latter are known, STA is extremely powerful [39]. However, in large systems, which are required for AQC, the eigenstates are generally unknown. In such cases, one can either use approximate STA solutions [18, 36, 46] or resort to alternative methods.

Here, we present an acceleration method for adiabatic protocols with QOC. Our algorithm finds pulses by optimizing a cost function that takes into account practical constraints, while simultaneously drawing the solution towards the instantaneous eigenstate. We generalize early work by Brif et al. [7], on optimizing qubit control in closed systems with gradient ascent pulse engineering (GRAPE) [30]. STIRAP pulses were optimized in [37] by minimizing the input power while maximizing the robustness within the subspace of STA solutions. Adiabatic entangling gates were optimized in Ref. [43] with the chopped random-basis (CRAB) quantum optimization technique, and in Ref. [21] with ensemble optimization that guarantees robust performance at the expense of expensive brute-force calculations. Finally, Ref. [11] proposes improving approximate STA with additional control fields. *In light of the recent literature, the contribution of the present method lies in its generality, efficiency, and applicability to multi-qubit, multi-level open systems.* To demonstrate the generality of our approach, we analyze its performance by running a digitized adiabatic protocol on the IBM quantum platform [25] and by running Python simulations of quantum annealing with Rydberg qubit arrays [15].

We begin by introducing our adiabatic optimization

* These authors contributed equally to this work.

† adi.pick@mail.huji.il

method for open quantum systems. Real quantum systems are open since they exchange energy and particles with their environment. Assuming a Markovian environment with relaxation rate faster than that of the system, the dynamics of the density matrix, ρ , is governed by the Lindblad master equation: [10]

$$\frac{d\rho}{dt} = -i [H(\mathbf{v}(t)), \rho] + \sum_k \left(\hat{L}_k \rho \hat{L}_k^\dagger - \frac{1}{2} \{ \hat{L}_k^\dagger \hat{L}_k, \rho \} \right). \quad (1)$$

The Hamiltonian H includes control and uncontrolled (drift) terms. The vector $\mathbf{v}(t)$ stores the control amplitudes and frequencies. The environment causes non-Hamiltonian “quantum jumps,” generated by the operators \hat{L}_k , including population relaxation and dephasing.

To accelerate adiabatic protocols, we seek pulse parameters $\mathbf{v}(t)$ that drive the system along the instantaneous ground state of H . To do so, we minimize the functional:

$$\mathcal{C}(\rho(t), \mathbf{v}(t), t_f) = \mathcal{C}_{\text{fid}} + \eta \mathcal{C}_{\text{power}}, \quad (2)$$

where η balances fidelity and power constraint, and t_f is the protocol duration. We consider three figures of merit for the fidelity:

$$C_{\text{fid}}^1 = 1 - \text{Tr} \sqrt{\sqrt{\rho_g(t_f)} \rho(t_f, \mathbf{v}(t)) \sqrt{\rho_g(t_f)}}, \quad (3a)$$

$$C_{\text{fid}}^2 = \frac{1}{t_f} \int_0^{t_f} dt \left(1 - \text{Tr} \sqrt{\sqrt{\rho_g(t)} \rho(t, \mathbf{v}) \sqrt{\rho_g(t)}} \right), \quad (3b)$$

$$C_{\text{fid}}^3 = \frac{1}{M} \sum_{i=1}^M u_i C_{\text{fid}}^1 \{ \rho_i(t), \mathbf{v}(t), \alpha_i \}. \quad (3c)$$

The term C_{fid}^1 quantifies the deviation of the system’s state at the end of the protocol, $\rho(t_f)$, from the desired eigenstate, $\rho_g(t_f)$, using the fidelity amplitude metric [40], where both states depend implicitly on $\mathbf{v}(t)$. We refer to C_{fid}^1 as the diabatic error, and to pulses obtained by minimizing it as traditional QOC. The term, C_{fid}^2 , is the accumulated diabatic error along the propagation, and we refer to pulses obtained by minimizing it as adiabatic QOC. *Our work compares the two methods (Fig. 1) and highlights advantages for adiabatic QOC.*

Finally, C_{fid}^3 is used for ensemble optimization. It is the average diabatic error, C_{fid}^1 , for an ensemble of systems, whose states $\rho_i(t)$ evolve under controls shifted or scaled by α_i , with u_i denoting the averaging weights. Specifically, we simulate ensembles of varying pulse amplitudes, frequencies, and relaxation rates. More details are given in the supplementary information (SI). Moreover, some of our calculations use C_{fid}^1 and C_{fid}^2 simultaneously. Finally, we restrict the pulse power via the minimizing its deviation from a reference value of \mathcal{C}_0 ,

$$\mathcal{C}_{\text{power}} = \max \left(\left| \sum_{\mu=1}^N \int_0^{t_f} v_\mu^2(t) dt - \mathcal{C}_0 \right|, 0 \right), \quad (4)$$

where the sum runs over all controls, stored as elements of \mathbf{v} . The maximum between $\mathcal{C}_{\text{power}}$ and 0 is minimized to allow finding pulses with pulse power smaller than \mathcal{C}_0 .

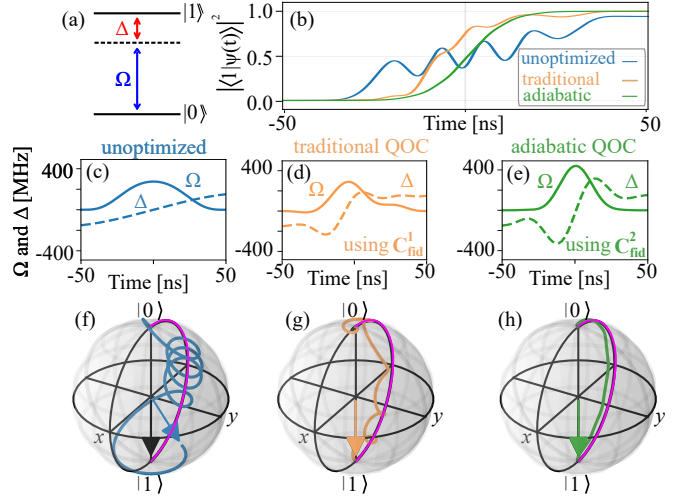


Fig. 1. Adiabatic optimization of RAP: (a) A two-level system, $\{|0\rangle, |1\rangle\}$, driven by a pulse with Rabi frequency Ω and detuning Δ . (b) Population in state $|1\rangle$ when evolving under the unoptimized polynomial pulse (c, blue); traditional QOC pulse (d, orange) and adiabatic QOC pulse (e, green). (f–h) Trajectory of the Bloch vector under pulses (c–e). Purple curve shows the instantaneous eigenstate.

We use the chopped random basis (CRAB) quantum optimization method to expand the control fields in a truncated basis of smooth, randomized functions [9]. We use three functional bases:

$$f^{(1)}(t) = f_0(t) + \sum_m w_m \exp \left(-\frac{(t-\mu_m)^2}{\sigma_m^2} \right), \quad (5a)$$

$$f^{(2)}(t) = f_0(t) + \sum_m w_m \sin \left(m\pi \cdot \frac{t+\tau}{2} \right), \quad (5b)$$

$$f^{(3)}(t) = f_0(t) + \sin^2 \left(\frac{\pi t}{t_f} \right) \cdot \sum_m w_m T_m \left(\frac{2t}{t_f} - 1 \right), \quad (5c)$$

where $f_0(t)$ is a fixed reference pulse and the sums represent corrections spanned in bases of Gaussians, sine functions, and Chebyshev polynomials, $T_m(z)$, respectively. The squared sine envelope in Eq. (5c) guarantees smoothness of the basis functions at the start and end of the protocol [47]. We optimize the cost functions [Eq. (3)] over the variables w_m in the sine and Chebyshev bases and w_m, μ_m, σ_m in the Gaussian basis.

We employ the CMA-ES algorithm [23] to perform the optimization. The algorithm begins with a set of guess solutions and iteratively updates the mean and covariance of the set to guide the search towards high-fidelity solutions. The optimization is carried out with the open-source Python library Nevergrad [4]. To solve the Lindblad master equation [Eq. (1)], we use the open-source Python package QuTiP [27]. To reduce the complexity of solving the Lindblad master equation for a multi-level, multi-particle open system, we employ the stochastic trajectory method [1, 10], which consists of averaging over solutions of an effective Schrödinger equation.

Next, we apply our optimization strategy to three adia-

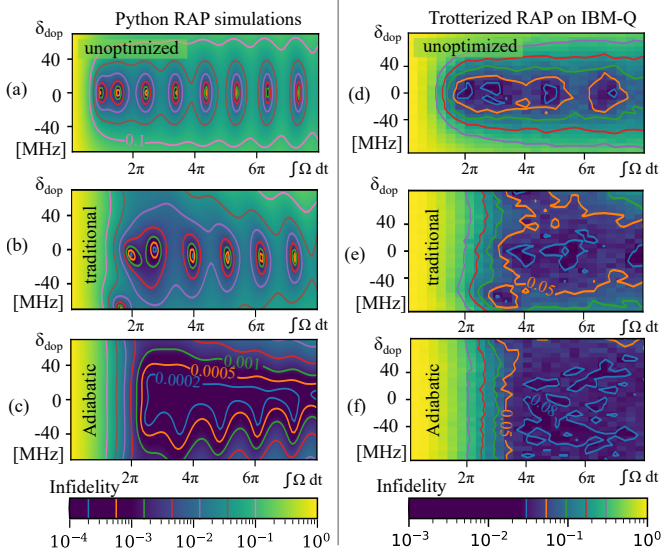


Fig. 2. Robustness of optimized RAP pulses. (a–c) Python simulations showing infidelity of state transfer [Eq. (3a)] (colorbar) for the three pulses from Fig. 1 under variations in pulse amplitude, $\int_0^{t_f} \varepsilon \Omega(t) dt$ and frequency shifts, $\Delta(t) + \delta_{\text{dop}}$. (d–f) Infidelity of a trotterized RAP protocol under variations in the controls pulse area and detuning, obtained from quantum simulations on the IBM quantum cloud [25].

batic protocols. Our first example is rapid adiabatic passage (RAP)—a protocol for population transfer between the ground and excited states of a two-level “qubit” system, by application of a chirped pulse. The Hamiltonian of a two-level system driven by a classical field in the rotating-wave approximation (RWA) is [20]

$$H_{\text{RAP}} = \Omega(t)\hat{\sigma}_x + \Delta(t)\hat{\sigma}_z, \quad (6)$$

where $\Omega(t)$ is the Rabi single-photon and $\Delta(t)$ is the frequency detuning of the field [Fig. 1(a)]. In RAP, Ω vanishes at the start and end of the protocol [Fig. 1(c)]. Therefore, H_{RAP} reduces to $\Delta\hat{\sigma}_z$, and since Δ flips sign at $t = 0$ and t_f , the instantaneous ground state, $|\psi_g(t)\rangle$, changes from $|0\rangle$ to $|1\rangle$. By adiabatically following $|\psi_g(t)\rangle$, population is transferred from $|0\rangle$ to $|1\rangle$.

To increase the state transfer fidelity under fixed time and energy constraints, we use the QOC framework just presented. We compare the dynamics under three pulses: (1) An “unoptimized” polynomial pulse, which consists of a sixth-order polynomial for $\Omega(t)$ and a cubic polynomial for $\Delta(t)$ [41], (2) A pulse obtained using “traditional QOC,” with C_{fid}^1 [Eq. (3a)] (orange), and (3) an “adiabatic QOC” pulse, obtained by combining C_{fid}^1 and C_{fid}^2 [Eq. (3b)] (green). The optimization is performed with a basis of sine functions [Eq. (5b)]. The evolution and pulses are shown in Fig. 1(b–e). Finally, the evolution of the Bloch vector is shown in Fig. 1(f–h), showing that only the pulse obtained from adiabatic QOC (green) adheres to the instantaneous eigenstate (purple).

Since the adiabatic QOC trajectory adheres to the instantaneous eigenstate, we expect robustness to fluctu-

ations in the control parameters. In Fig. 2, we consider variations in the pulse amplitude and frequency. Given a pulse with Rabi frequency $\Omega_0(t)$ and detuning $\Delta_0(t)$, we evolve the system and compute the infidelity under a perturbed pulse with a rescaled Rabi frequency, $\Omega_0(t) \rightarrow \epsilon \Omega_0(t)$, and a shifted detuning, $\Delta_0 \rightarrow \Delta_0 + \delta_{\text{dop}}$. These noise sources are prevalent in coherent control of atomic clouds due to variations in atomic position and motion [29]. (Robustness to variations in qubit lifetimes is discussed in the next example, which studies STIRAP.)

Figure 2(a–c) shows the robustness of the three pulses from Fig. 1 by plotting the infidelity, C_{fid}^1 , (colorbar) as a function of the frequency offset δ_{dop} and pulse area $\int_0^{t_f} \Omega(t) dt$. Both the unoptimized polynomial pulse and the pulse obtained from traditional QOC show islands of high fidelity (dark blue) upon increasing the Rabi frequency resulting from Rabi oscillations, and a sharp fidelity drop for non-zero Doppler shifts. However, the pulse obtained from adiabatic QOC achieves high state-transfer fidelity over a range of pulse areas and Doppler shifts (blue region). To verify our results on real quantum hardware, we ran a digitized (trotterized) version of RAP on IBM’s online quantum platform [25]. We generated 625 Hamiltonian parameters, with 25 Doppler shifts and 25 pulse areas, and performed the trotterized RAP for each parameter set and each one of the pulses from Fig. 1. The average infidelity over 1024 computations is shown in Fig. 2(d–f). The results of the quantum trotterized RAP computations show a similar trend as the Python results, but the fidelity is lower since we perform 1024 repetitions for each parameter set, and the statistical error decreases the overall fidelity. In the SI, we compare our method with ensemble optimization. While both methods find pulses that are robust to Doppler shifts and intensity variations, adiabatic optimization is more efficient.

Next, we accelerate an extended STIRAP protocol for state transfer between two superconducting qubits mediated via a multimode waveguide presented in Refs. [12, 34]. We analyze the robustness of the pulses under varying qubit and guided-mode lifetimes. To benchmark our method, we compare the performance of adiabatic QOC with an STA method called super-adiabatic transitionless driving (SATD), which relies on eliminating diabatic errors in the instantaneous eigenvector basis [3]. The system from Ref. [12] consists of two qubits, which are coupled to a multimode waveguide via tunable couplers [Fig. 3(a)]. Qubits A and B are coupled to the n^{th} mode of the waveguide with amplitudes $g_{ac}^n(t)$ and $g_{bc}^n(t)$ respectively. Considering the single-excitation subspace (i.e., neglecting multiphoton excitations in the connector), the system’s Hamiltonian is [34, 44]:

$$H_{\text{STIRAP}} = \sum_n \left\{ \Delta_n |0_a 0_b 1_c^{(n)}\rangle \langle 0_a 0_b 1_c^{(n)}| + g_{ac}^n(t) |1_a 0_b 0_c\rangle \langle 0_a 0_b 1_c^{(n)}| + g_{bc}^n(t) |0_a 1_b 0_c\rangle \langle 0_a 0_b 1_c^{(n)}| + \text{h.c.} \right\}. \quad (7)$$

The notation $|1_a 0_b 0_c\rangle$ indicates that qubits A and B are in $|1\rangle$ and $|0\rangle$ respectively, and all guided modes have

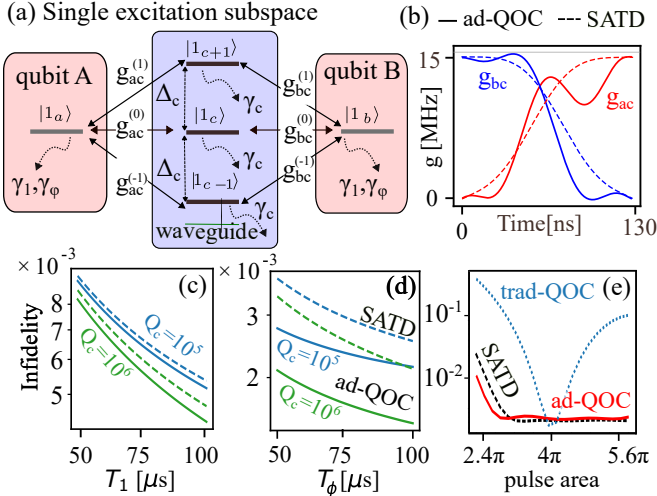


Fig. 3. (a) The single-excitation subspace of two qubits coupled to a multimode waveguide with couplings $g_{ac}^{(n)}$ and $g_{ab}^{(n)}$. Decay rates $\gamma_1, \gamma_\phi, \gamma_c$ corresponding to qubit relaxation, dephasing, and photon decay, while Δ_c is the FSR. (b) Coupling amplitudes $g_{ac}(t)$ (red) and $g_{ab}(t)$ (blue) of SATD (dashed) and adiabatic QOC (solid). (c) Infidelity of state transfer, C_{fid} for varying T_1 relaxation times under SATD (dashed) and adiabatic QOC (solid) for quality factors $Q_c = 10^5$ (blue) and $Q = 10^6$ (green). (d) Similar to (c) for dephasing lifetime, T_ϕ . (e) Infidelity of SATD (dotted), adiabatic (solid) and traditional QOC (black) pulses when varying the pulse area of the couplings from (b).

zero photons. Similarly, $|0_a 0_b 1_c^{(n)}\rangle$ indicates that both qubits are in $|0\rangle$, the n^{th} guided mode contains a single photon, while all other modes are empty. We use $\Delta_n = n\Delta_c$ to denote the detuning of the coupling to the n^{th} guided mode, with $n \in \mathbb{Z}$ and Δ_c denoting the free spectral range (FSR) of the waveguide. We assume that the coupling coefficients $g_{ab}^{(n)}, g_{ac}^{(n)}$ are equal in magnitude for all n and have alternating signs [$\propto (-1)^n$] when the parity of guided modes alternates between even and odd.

When $\Delta_c \gg g_{ab}^{(n)}, g_{ac}^{(n)}$, only the resonant $n = 0$ mode couples to the qubits and the single-excitation subspace contains three levels, as in traditional STIRAP. The Hamiltonian has a “dark state,” containing zero photons,

$$|D(t)\rangle = \cos\theta(t)|1_a 0_b 0_c\rangle - \sin\theta(t)|0_a 1_b 0_c\rangle, \quad (8)$$

with $\theta(t) \equiv \tan^{-1}[g_{ac}(t)/g_{bc}(t)]$. The dark state changes from $|1_a 0_b 0_c\rangle$ to $|0_a 1_b 0_c\rangle$ by changing $\theta(t)$ from 0 to $\pi/2$, i.e., by applying first $g_{bc}(t)$ and then $g_{ac}(t)$ [Fig. 3(b)]. STIRAP relies on adiabatically following $|D(t)\rangle$. To accelerate STIRAP, one can use that SATD pulses [34]

$$\begin{aligned} g_{ac}^{\text{SATD}}(t) &= g \left(\sin\theta(t) + \frac{\cos[\theta(t)]\ddot{\theta}(t)}{g^2 + \dot{\theta}(t)^2} \right) \\ g_{bc}^{\text{SATD}}(t) &= g \left(\cos\theta(t) - \frac{\sin[\theta(t)]\ddot{\theta}(t)}{g^2 + \dot{\theta}(t)^2} \right), \end{aligned} \quad (9)$$

shown in Fig. 3(b) (dashed). In the limit of large FSR,

SATD pulses give excellent performance since they are obtained by analytically eliminating diabatic errors.

However, when the FSR is comparable to the coupling amplitudes $\Delta_c \simeq \max(g_{ab}^{(n)}, g_{ac}^{(n)})$, the SATD solution is not exact. The next-order approximation to the dynamics includes the nearest sideband modes ($n \pm 1$), and the single excitation subspace contains five levels. The Hamiltonian has a quasi dark state [34]

$$\begin{aligned} |D^{(1)}(t)\rangle &\propto \cos(\theta)|1_a 0_b 0_c\rangle - \sin(\theta)|0_a 1_b 0_c\rangle + \\ &\frac{\sin(2\theta)g(t)}{\Delta}|0_a 0_b 1_c^{(-1)}\rangle + \frac{\sin(2\theta)g(t)}{\Delta}|0_a 0_b 1_c^{(1)}\rangle. \end{aligned} \quad (10)$$

The second line contains the bright-state (single-photon) wavefunction components, which are suppressed by increasing the ratio $|g(t)|/\Delta_c$, where $g \equiv \sqrt{g_{ac}^2 + g_{bc}^2}$. A pulse obtained with adiabatic QOC, i.e. optimizing the adherence to $|D^{(1)}(t)\rangle$ using a basis of Chebyshev polynomials [Eq. (5c)] is shown in Fig. 3(b) (solid).

We compare the state-transfer infidelity for SATD and adiabatic QOC pulses under varying relaxation (T_1) and dephasing (T_ϕ) lifetimes. To do so, we first find the optimal pulse envelopes, $g_{ab}(t)$ and $g_{ac}(t)$, assuming $T_1 = 50 \mu\text{s}$, and then evolve the system under these envelopes to compute the infidelity over a range of T_1 values. In Fig. 3(d), we repeat these steps for dephasing noise. In both cases, we denote the decay rate of single-photon states, $\gamma_c = \omega_c/Q_c$, by the corresponding quality factor Q_c , with $\omega_c = 5 \text{ GHz}$. The adiabatic QOC pulse (solid curves) outperforms SATD pulses (dashed) for both quality factors and all qubit lifetimes in the shown range. In Fig. 3(e), we test the robustness to amplitude fluctuations by scaling the amplitude of the optimized and SATD pulses by an overall scale factor, replacing $g^{(n)} \rightarrow \epsilon g^{(n)}$. Here, $T_1 = T_\phi = 100 \mu\text{s}$ and $Q = 10^5$. The performance of adiabatic QOC and SATD is almost identical, but both are more robust than traditional QOC, as expected (dotted).

Our final example is an AQC for finding the MIS of a graph. Following Refs. [15, 31, 42], we implement an algorithm that uses Rydberg qubits—two-level atoms with a low-energy hyperfine state and a high-excitation Rydberg state [Fig. 4(a)]. Rydberg states have a large dipole moment, which prevents atoms with mutual distance less than a critical “blockade radius” r_B from being simultaneously excited. A lattice of Rydberg qubits can represent a graph, $G(N, E)$, where each qubit corresponds to a node $i \in N$, and nodes represented by qubits with mutual distance $d < r_B$ are connected by an edge $(i, j) \in E$. The AQC for finding the MIS of $G(N, E)$ proceeds as follows: All qubits are initialized in the ground state. Then, a global RAP pulse is applied, attempting to excite all atoms. Rydberg blockade prohibits excitations of qubits with mutual distance $d < r_B$, so the system naturally finds the maximum number of allowed Rydberg excitations—corresponding to the MIS of $G(N, E)$.

To test our method, we optimize an AQC for finding the MIS of ring graphs with an even number of nodes. The MIS is known—consisting of every other

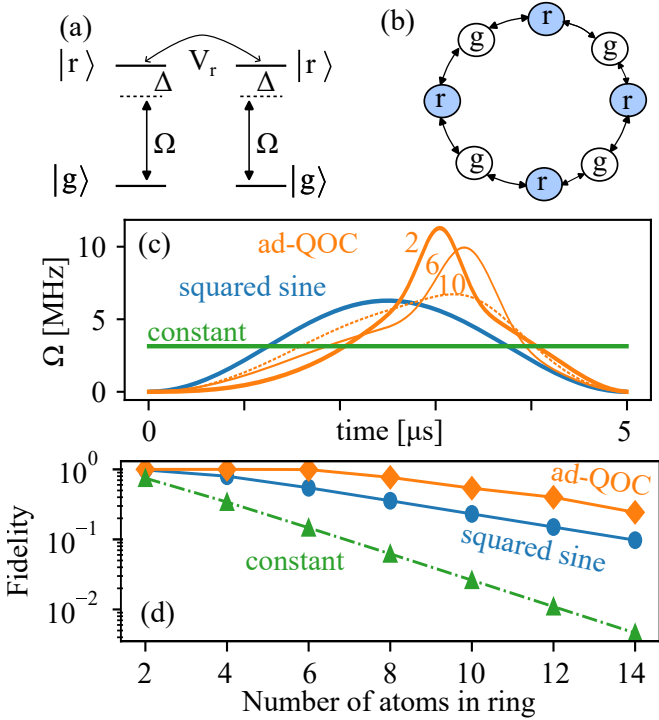


Fig. 4. (a) Rydberg qubits with levels $|g\rangle$ and $|r\rangle$. V_r is the Rydberg interaction, while Ω and Δ are the Rabi frequency and detuning of the control. (b) An 8-node ring graph and one of its MIS solutions. (c) Rabi frequency $\Omega(t)$ of a constant field (green), a squared sine pulse (blue), and pulses obtained with adiabatic QOC for rings containing $N = 2, 6, 10$ atoms (orange). (g) Overlap of the final state and MIS solution, $1 - C_{\text{fid}}^1$, versus ring length for the pulses from (c).

node [Fig. 4(b)]—and is used to evaluate the error of the AQC. Under the simplifying assumption that only nearest neighbors in the ring interact, the Hamiltonian is

$$H_{\text{MIS}} = \sum_{i \in N} [\Omega(t) \hat{\sigma}_x^i - \Delta(t) \hat{\sigma}_z^i] + V_r \sum_{(i,j) \in E} \hat{n}_i \hat{n}_j, \quad (11)$$

where the first sum represents the global RAP pulse, with $\Delta(t)$ a cubic polynomial swept from positive to negative, and $\Omega(t)$ an optimized pulse, shown in Fig. 4(c). The second sum represents Rydberg interactions, with V_r the Rydberg interaction strength and \hat{n}_i the projector of qubit i onto the Rydberg state, i.e., the product $\hat{n}_i \hat{n}_j$ is non-zero when both i and j are excited.

We compare the error in finding the MIS using AQC with the pulses from Fig. 4(c): A constant Rabi intensity (green), a squared sine pulse (blue), and pulses obtained from adiabatic QOC for rings containing $2, \dots, 14$ atoms (orange). (For clarity, only 3 optimized pulses are shown.) Starting from the squared sine pulse (blue), we search for pulses that minimize the adiabatic cost function, C_{fid}^2 , within a basis of shifted Gaussian functions [Eq. (5a)]. Since optimization becomes intractable for large rings, we reduce the Hilbert space dimension by projecting the Hamiltonian onto the subspace of states

without neighboring Rydberg excitations [42]. All simulations in Fig. 4(c) are obtained with pulses that have a pulse area of 4π . This is achieved by normalizing the pulse area of the optimized pulses prior to running the AQC. Fig. 4(d) shows the fidelity, $1 - C_{\text{fid}}^1$, as a function of chain length for the pulses from (c), demonstrating the optimal performance of pulses obtained with adiabatic QOC. For short chains ($N = 2, \dots, 8$) we find slightly asymmetric pulses (orange), while for longer chains, the asymmetry becomes less pronounced. Details about the convergence of our algorithm are given in the SI.

In summary, we proposed a useful approach for optimization of adiabatic protocols, which we call *adiabatic QOC*. Our pulse engineering method seeks pulses under which the evolving system adheres to the instantaneous eigenstate along the propagation. Our main findings can be summarized as follows. RAP pulses obtained from adiabatic QOC are more robust than traditional QOC, which seeks pulses that reach a target state with maximal fidelity [Fig. 2]. For state transfer in an open system, adiabatic QOC that takes into account the system openness outperforms STA solutions (SATD)—engineered to eliminate diabatic errors in closed systems [Fig. 3]. In the SI, we show that the robustness of the pulses obtained with adiabatic QOC is comparable to that of brute-force ensemble optimization, but our approach is more efficient. Finally, adiabatic QOC is applicable for intermediate-size systems, and we used it to optimize an AQC with a 14-qubit atom array [Fig. 4].

We conclude by mentioning directions for further research. Adherence to the instantaneous ground state along the propagation requires knowledge of the state, which is not available in large-scale AQC. Nevertheless, we hypothesize that AQC can be improved by seeking pulses that adhere to approximate ground states or by using knowledge of the ground state during early stages of the protocol. Furthermore, optimization of AQC requires classical computation resources in the optimization stage and quantum resources in the evolution stage. Understanding the tradeoff between classical and quantum complexities in adiabatic QOC is a question that requires further investigation.

Acknowledgment: AP acknowledges support from the Israel Science Foundation Grant No. 1484/24 and the Alon Fellowship of the Israeli Council of Higher Education. The authors thank Prof. Nir Davidson, Prof. Ofer Firstenberg, and Amit Tsabari for insightful discussions on noise sources in atom interferometry. The authors thank Dr. Haggai Landa for discussions on noise sources in the IBM quantum platform. Finally, the authors thank Nadav Avtar and Dor Atias for support with the digitized RAP code.

SUPPLEMENTARY INFORMATION FOR PULSE OPTIMIZATION IN ADIABATIC QUANTUM COMPUTATION AND CONTROL

This supplementary information presents two analyses related to the optimization framework developed in the main text. In the first part, we compare ensemble-based optimization and adiabatic quantum optimal control (QOC) in the context of rapid adiabatic passage (RAP). We validate the performance of both approaches through numerical simulations and experimental implementation on IBM quantum hardware. In the second part, we analyze the convergence behavior of adiabatic QOC when applied to solving the Maximum Independent Set (MIS) problem on ring graphs. Focusing on representative cases with $N = 8, 10$, and 12 atoms, we track the evolution of fidelity and pulse area penalty over the course of the optimization.

I. COMPARISON BETWEEN ENSEMBLE OPTIMIZATION AND ADIABATIC QOC

In this work, we compare the performance of adiabatic QOC (see main text) and ensemble QOC. Adiabatic QOC directly minimizes the time-integrated diabatic error, C_{fid}^2 [Eq. (3, b)], steering the system to follow the instantaneous ground state throughout the evolution. By contrast, ensemble optimization minimizes the weighted-average terminal diabatic error, C_{fid}^3 [Eq. (3, c) [21]], across an ensemble of Hamiltonians with perturbed amplitudes, detunings, or lifetimes to ensure robustness against parameter fluctuations. The principal benefit of adiabatic QOC is its dramatic reduction in classical optimization runtime while achieving comparable robustness.

Physically, spatial inhomogeneities in our control beams and residual atomic motion give rise to two dominant error channels in RAP implementations: variations in the integrated pulse area and Doppler-induced detuning offsets. An atom displaced off-axis experiences a reduced Rabi frequency, while thermal velocities detune the drive. Demonstrating that adiabatic QOC pulses maintain high fidelity across these amplitude and frequency fluctuations confirms that our optimization protocol is resilient to the primary noise sources encountered in realistic laboratory quantum-control experiments.

A detailed comparison of the robustness landscapes obtained via adiabatic QOC [Eq.(3, b)] and ensemble optimization [Eq.(3, c)] is presented in Fig. S1. In Python simulations (Fig. S1,a–b), both schemes yield nearly identical high-fidelity regions across the pulse-area–Doppler-shift plane, with infidelities remaining below 10^{-3} over the central plateau. Trotterized experiments on IBM hardware (Fig. S1,c–d) reproduce these trends, confirming that the optimized pulses perform equally well in the laboratory. Although the robustness landscapes are nearly identical, the classical runtime differs dramatically: all CMA-ES optimizations were run single-threaded on an ASUS laptop with an Intel Core Ultra 9 185H processor (16 cores, 22 threads @ 2.50 GHz base, 32 GB RAM) under Windows 11 Home 24H2. Using a fixed budget of 2000 CMA-ES iterations, adiabatic QOC completed in ~ 2 min, whereas ensemble optimization—evaluated over a 5×5 grid of pulse areas and Doppler shifts at the same budget—required ~ 40 min, underscoring the superior computational efficiency of adiabatic QOC

To verify the robustness of our optimized pulses on real quantum hardware, we digitized the continuous RAP Hamiltonian using a second-order Trotter decomposition [45] and executed the resulting circuits on IBM Quantum. In our Qiskit implementation, the instantaneous unitary

$$U(t_k + \Delta t, t_k) = \exp(-i H(t_k) \Delta t), \quad H(t_k) = \Omega(t_k) \sigma_x + \Delta(t_k) \sigma_z, \quad \Delta t = t_{k+1} - t_k. \quad (12)$$

was approximated via the symmetric second-order Suzuki–Trotter decomposition [45]:

$$\exp(-i H(t_k) \Delta t) \approx R_z(\Delta(t_k) \Delta t/2) R_x(\Omega(t_k) \Delta t) R_z(\Delta(t_k) \Delta t/2). \quad (13)$$

Here, $R_x(\theta) = e^{-i \theta \sigma_x/2}$ and $R_z(\phi) = e^{-i \phi \sigma_z/2}$ denote single-qubit rotations about the x - and z -axes, respectively. implemented via Qiskit’s `rz` and `rx` gates in the `trot_circuit` routine.

All 625 parameter-sweep circuits were transpiled for the IBM Quantum backend `ibm_brisbane` (7-qubit heavy-hex topology) accessed through `QiskitRuntimeService` [25]. For consistency across runs, each single-qubit circuit was pinned to physical qubit 3, with optimization level 0 and measurement in the Z-basis. The resulting infidelity landscape (Fig. S1c–d) closely matches our Python simulations, confirming that the digitized adiabatic pulses retain their designed robustness under the native gate set and noise characteristics of real hardware.

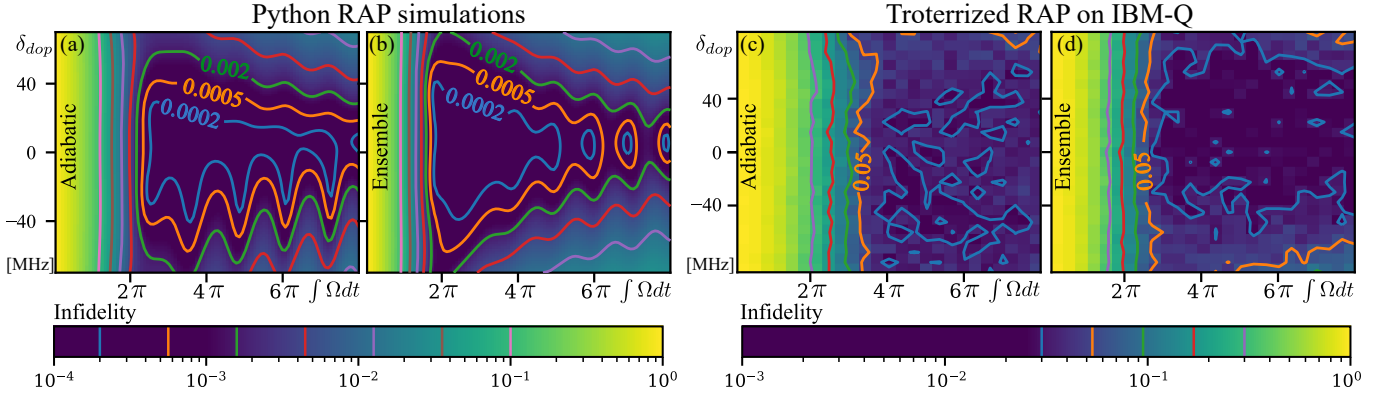


Fig. S1. Robustness of RAP pulses. (a,b) Python simulations showing infidelity of state transfer fidelity (see colorbar), as a function of pulse area and Doppler shift for pulses optimized via adiabatic QOC [Eq.(3, b)] (a) and ensemble optimization [Eq.(3, c)] (b). (c,d) Trotterized RAP experiments on IBM hardware [25] for the same two optimization schemes: adiabatic QOC (c) and ensemble (d).

II. ANALYSIS OF CONVERGENCE OF ADIABATIC QOC FOR RING GRAPHS

In the main text, we apply adiabatic quantum optimal control (QOC) to solve the Maximum Independent Set (MIS) problem on ring graphs of length $N = 2$ to 14. Here, we analyze the convergence behavior of the optimization algorithm for three instances with $N = 8, 10$, and 12 atoms. To monitor optimization progress, we track the fidelity at each iteration. The control pulse is parameterized using a sum of seven Gaussian basis functions see Eq. 5c in the main text, with each Gaussian defined by an amplitude, width, and temporal offset, yielding a 21-dimensional optimization space.

Figure (S2) shows the cost function terms as a function of iteration number of rings containing $N = 8, 10$ and 12 nodes. The top row displays both raw and moving-averaged traces of the area penalty, and the bottom row shows the fidelity on a linear scale. Across all three values of N , we observe two characteristic thresholds in convergence: an initial point where the infidelity begins to drop significantly, and a later stage where it stabilizes near its final value. Both thresholds shift to later iterations for larger N , indicating increased complexity in the optimization landscape.

In the main text, the area of the pulses obtained from the optimization algorithm is renormalized before running the AQC. We do so in order to compare the performance of pulses that have an equal pulse area. The infidelity values shown in Fig. (S2) (bottom) correspond to the pulses before renormalizing their area. This explains the slight deviation between the infidelity values shown here and in the main text.

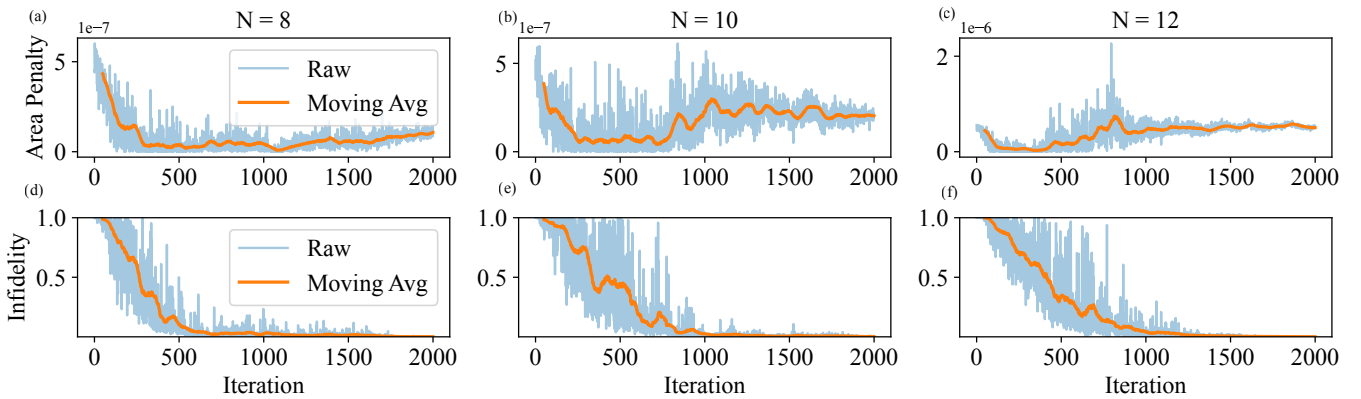


Fig. S2. Convergence behavior of the optimization process for $N = 8, 10$, and 12 atoms. Panels (a)–(c) show the evolution of the area penalty over 2000 iterations, while panels (d)–(f) display the corresponding infidelity. Both raw values and moving averages (window size 50) are shown. For all instances, the optimization exhibits improvement, with final fidelities approaching unity.

[1] Abdelhafez, M., D. I. Schuster, and J. Koch (2019), Physical Review A **99** (5), 052327.

[2] Albash, T., and D. A. Lidar (2018), Reviews of Modern Physics **90** (1), 015002.

[3] Baksic, A., H. Ribeiro, and A. A. Clerk (2016), Physical review letters **116** (23), 230503.

[4] Bennet, P., C. Doerr, A. Moreau, J. Rapin, F. Teytaud, and O. Teytaud (2021), ACM SIGEVolution **14** (1), 8.

[5] Berry, M. V. (2009), Journal of Physics A: Mathematical and Theoretical **42** (36), 365303.

[6] Born, M., and V. Fock (1928), Zeitschrift für Physik **51** (3-4), 165.

[7] Brif, C., M. D. Grace, M. Sarovar, and K. C. Young (2014), New Journal of Physics **16** (6), 065013.

[8] del Campo, A. (2013), Physical Review Letters **111** (10), 100502.

[9] Caneva, T., T. Calarco, and S. Montangero (2011), Physical Review A **84** (2), 022326.

[10] Carmichael, H. (2009), *An open systems approach to quantum optics: lectures presented at the Université Libre de Bruxelles, October 28 to November 4, 1991*, Vol. 18 (Springer Science & Business Media).

[11] Čepaité, I., A. Polkovnikov, A. J. Daley, and C. W. Duncan (2023), PRX Quantum **4** (1), 010312.

[12] Chang, H.-S., Y. Zhong, A. Bienfait, M.-H. Chou, C. R. Conner, É. Dumur, J. Grebel, G. A. Pairs, R. G. Povey, K. J. Satzinger, *et al.* (2020), Physical Review Letters **124** (24), 240502.

[13] Claeys, P. W., M. Pandey, D. Sels, and A. Polkovnikov (2019), Physical review letters **123** (9), 090602.

[14] Dann, R., and R. Kosloff (2021), Physical Review Research **3** (1), 013064.

[15] Ebadi, S., A. Keesling, M. Cain, T. T. Wang, H. Levine, D. Bluvstein, G. Semeghini, A. Omran, J.-G. Liu, R. Samajdar, *et al.* (2022), Science **376** (6598), 1209.

[16] Evered, S. J., D. Bluvstein, M. Kalinowski, S. Ebadi, T. Manovitz, H. Zhou, S. H. Li, A. A. Geim, T. T. Wang, N. Maskara, *et al.* (2023), Nature **622** (7982), 268.

[17] Farhi, E., J. Goldstone, S. Gutmann, and M. Sipser (2000), arXiv preprint quant-ph/0001106.

[18] Finžgar, J. R., S. Notarnicola, M. Cain, M. D. Lukin, and D. Sels (2025), arXiv preprint arXiv:2503.01958.

[19] Garcia, L., J. M. Bofill, I. d. P. Moreira, and G. Albareda (2022), Physical Review Letters **129** (18), 180402.

[20] Gerry, C. C., and P. L. Knight (2023), *Introductory quantum optics* (Cambridge university press).

[21] Goerz, M. H., E. J. Halperin, J. M. Aytac, C. P. Koch, and K. B. Whaley (2014), Physical Review A **90** (3), 032329.

[22] Guérin, S., S. Thomas, and H. Jauslin (2002), Physical Review A **65** (2), 023409.

[23] Hansen, N. (2006), in *Towards a New Evolutionary Computation*, Studies in Fuzziness and Soft Computing, Vol. 192, edited by J. A. Lozano, P. Larrañaga, I. Inza, and E. Bengoetxea (Springer) pp. 75–102.

[24] Harutyunyan, M., F. Holweck, D. Sugny, and S. Guérin (2023), Physical Review Letters **131** (20), 200801.

[25] IBM Quantum, (2025), “Ibm quantum cloud,” <https://quantum.ibm.com>, accessed: June 2025.

[26] Jandura, S., and G. Pupillo (2022), Quantum **6**, 712.

[27] Johansson, J. R., P. D. Nation, and F. Nori (2012), Computer Physics Communications **183** (8), 1760.

[28] Jozsa, R. (1994), Journal of modern optics **41** (12), 2315.

[29] Kasevich, M., and S. Chu (1991), Physical review letters **67** (2), 181.

[30] Khaneja, N., T. Reiss, C. Kehlet, T. Schulte-Herbrüggen, and S. J. Glaser (2005), Journal of Magnetic Resonance **172** (2), 296.

[31] Kim, K., M. Kim, J. Park, A. Byun, and J. Ahn (2024), Scientific Data **11** (1), 111.

[32] Kolodrubetz, M., D. Sels, P. Mehta, and A. Polkovnikov (2017), Physics Reports **697**, 1.

[33] Lim, R., and M. Berry (1991), Journal of Physics A: Mathematical and General **24** (14), 3255.

[34] Malekakhlagh, M., T. Phung, D. Puzzuoli, K. Heya, N. Sundaresan, and J. Orcutt (2024), Physical Review Applied **22** (2), 024006.

[35] Møller, D., L. B. Madsen, and K. Mølmer (2007), Physical Review A **75** (6), 062302.

[36] Morawetz, S., and A. Polkovnikov (2025), arXiv preprint arXiv:2503.01952.

[37] Mortensen, H. L., J. J. W. Sørensen, K. Mølmer, and J. F. Sherson (2018), New Journal of Physics **20** (2), 025009.

[38] In this work, we seek pulses with integrated power of 4π [34].

[39] A widely used related method is derivative removal by adiabatic gate (DRAG) for reducing leakage in superconducting qubits.

[40] We used the QuTip built-in function to compute the fidelity amplitude. The traditional Uhlmann fidelity [28] is the square of the QuTip fidelity amplitude.

[41] The polynomial pulses we use are: $\Omega(t) = A - B \left(\frac{t}{\tau}\right)^4 + C \left(\frac{t}{\tau}\right)^6$ and $\Delta(t) = a \left(\frac{t}{\tau}\right) - b \left(\frac{t}{\tau}\right)^3$ with $A = 1, B = 3, C = 2, a = 0.6875, b = 0.1375$, chosen to have vanishing slopes and curvature at the start and end of the protocol, before normalizing the pulse area to 4π .

[42] Pichler, H., S.-T. Wang, L. Zhou, S. Choi, and M. D. Lukin (2018), arXiv preprint arXiv:1808.10816.

[43] Saffman, M., I. Beterov, A. Dalal, E. Páez, and B. Sanders (2020), Physical Review A **101** (6), 062309.

[44] Schwartzman-Nowik, Z., L. Shirizly, and H. Landa (2025), Physical Review A **111** (2), 022613.

[45] Suzuki, M. (1976), Communications in Mathematical Physics **51** (2), 183.

[46] Takahashi, K., and A. del Campo (2024), Physical Review X **14** (1), 011032.

[47] Turyansky, D., O. Ovdat, R. Dann, Z. Aqua, R. Kosloff, B. Dayan, and A. Pick (2024), Physical Review Applied **21** (5), 054033.

[48] Vitanov, N. V., A. A. Rangelov, B. W. Shore, and K. Bergmann (2017), Reviews of Modern Physics **89** (1), 015006.

[49] Žunkovič, B., P. Torta, G. Pecci, G. Lami, and M. Collura (2025), Physical Review Letters **134** (13), 130601.